3D printed temperature-sensing repairs for concrete structures

Christos Vlachakis[*], Marcus Perry, Lorena Biondi and Jack McAlorum

Department of Civil and Environmental Engineering, University of Strathclyde, Glasgow, G1 1XJ, UK

*Corresponding author. email address: christos.vlachakis@strath.ac.uk

Abstract

Multifunctional coating materials have enjoyed extensive development within civil engineering in the last few decades, with numerous proposals for self-sensing and self-healing repairs. Less thought has been afforded to coating material deployment, but a reliance on conventional manual methods is leading to high costs and variabilities in performance. This is prohibiting the application of new materials in the field. This paper addresses this issue by outlining, for the first time a 3D printable temperature sensing repair for concrete. The multifunctional material used in this study is a geopolymer: a durable alternative to ordinary Portland cement repairs, which can be electrically interrogated to act as a sensor. In this paper, we outline the material and 3D printing process development, and demonstrate 3D printed repair patches with a temperature sensing precision of 0.1 °C, a long-term sensing repeatability of 0.3 °C, a compressive strength of 24 MPa, and an adhesion strength to concrete of 0.6 MPa. The work demonstrates the feasibility of using additive manufacturing as a new means of applying repairs to concrete substrates, and provides one clear pathway to removing some of the barriers to the field deployment of multifunctional materials in a civil engineering context. The process shown here could enhance the design versatility of self-sensing repairs, unlock remote deployment, and de-cost and de-risk actions that prolong the lifespan and performance of existing concrete structures.

Keywords: geopolymer; additive manufacturing; smart material; temperature sensor; repair

1. Introduction

Geopolymers are a class of alkali activated materials that have gained popularity as a low-carbon alternative to ordinary Portland cement (OPC) [1,2]. Geopolymers exhibit similar mechanical properties to OPC, but a higher electrolytic conductivity due to free ions in their matrix [3,4]. This has allowed geopolymers to be developed for a wide array of multifunctional applications, ranging from the production of concrete elements [5–8], to fire- and chloride- resistant repair and coating systems [9–14], to sensing applications [15–22].

OPC and geopolymer concrete systems have seen some applications within 3D printing, primarily to produce structural elements via extrusion, direct ink writing and powder-bed processes [23–27]. Despite these applications, at the time of writing, the use of geopolymers as 3D printed multifunctional *coatings* for concrete has not been studied in detail. There are, however, clear benefits to 3D printing multifunctional sensor-repair coatings onto concrete substrates:

i) when compared to manual methods, additive manufacturing methods, like 3D printing, can improve the repeatability of deposition and hence the repeatability of repair and sensor performance;
ii) 3D printing reduces labour costs, and provides fixed marginal costs per printed item;
iii) interfacing 3D printing with robotics could allow sensor-repairs to be deployed in harsh, dangerous or remote environments without risk to personnel.

This paper outlines the 3D printing of metakaolin geopolymer sensor-repairs onto concrete substrates. We discuss and test the adhesion of the patch, its temperature-sensing capability, and the challenges in development. As far as we are aware, this is the first time that 3D printable self-sensing repairs for concrete substrates have been demonstrated.

Applications for this technology include remotely-deployable, retrofitted repairs and continuous monitoring solutions for existing structures in hazardous construction, nuclear or oil and gas environments. The technology could also be deployed within the precast sector. In either case, facilitating cheap, low-risk, continuous data acquisition could contribute to a clearer understanding of concrete structural health and design.

This paper begins with a brief introduction to geopolymer fabrication, coatings and sensing. Following this the state of the art in the 3D printing of cementitious materials is outlined. Thereafter the materials and methodology used in this research are presented, and the 3D printing process and performance of the patches as sensors and repairs are outlined.

2. Background and theory

2.1 Geopolymer fabrication and raw materials

Geopolymers are alkali-activated materials with an amorphous to semi-crystalline three dimensional silico-aluminate structure. They are usually formulated with a two-part mix of: i) a solid aluminosilicate precursor, typically metakaolin (calcined clay), fly ash and blast furnace slag [28]; and ii) an alkaline solution, a mixture of an alkali hydroxide and silicate solution typically sodium or potassium based [29]. When the precursor and the alkaline solution are mixed together the process of alkaline activation (or geopolymerisation) is initiated, and a series of reactions transpire — namely dissolution, rearrangement, condensation and solidification [30].

In this work, we have opted to use a metakaolin precursor and a sodium-based activator. Metakaolin is an amorphous material formulated through the calcination of kaolin (china clay) at temperatures of 550 – 850 °C. During heat treatment, the clay is dehydroxylated and the structure of kaolin is disordered into metakaolin, our reactive precursor [2,31]. Metakaolin was chosen in this work as it:

i) tends to be more compositionally consistent and more reactive than fly ash [30];
ii) is a raw material, whereas fly ash is an inconsistent industrial by-product of coal combustion, a globally dwindling industry;
iii) produces more suitable repairs than blast furnace slag geopolymers [14].

Metakaolin geopolymers do, however, tend to have a lower workability than fly ash geopolymers. This is due to their disc-shaped particles [32].

2.2 Geopolymer coatings for concrete

OPC substrates, such as concrete, consist of rich calcium-based surfaces which react with geopolymers to form a strong chemical bond between the two materials. [33]. This is a clear benefit for a coating and repair material, but one that can raise its own challenges. Geopolymers shrink during curing, and this can cause stress to develop when the coating is restrained by adhesion. If the layer of geopolymer coating is thin, tensile stresses can surpass the instantaneous strength of the curing geopolymer, causing cracks to appear. Thicker coating layers, meanwhile, are more susceptible to stresses at the substrate-coating interface, and this can cause de-bonding [34]. Potential means of mitigating high shrinkage levels in repair materials include the incorporation of sand [12,35,36], fibres - polypropylene (PP) [12,35], polyvinyl alcohol (PVA) [9], expansion reagents [35] and nanoparticles for refining the microstructure [37].

The concrete substrate's moisture levels and surface conditions also play a role. Substrates which are too dry or wet can absorb or supply water respectively, unbalancing any optimisations made in the chemical composition of the geopolymer binder [38]. For this reason, consistent methods of pre-wetting concrete substrates and removing excess surface water prior to geopolymer deposition are vital [39]. Finally, in order to ensure proper performance of a repair, suitable surface preparation is required. Rough surfaces are preferred in these cases as this leads to greater bond strength [40,41]. Among the many available surface treatment methods, sand-blasting and wire brushing have been proven to be the most effective [42].

2.3 Geopolymer electrical conductivity

Due to the alkaline solution in their pores, geopolymers are solid electrolytic conductors which exhibit a reasonably high electrical conductivity of order 10^{-4}-10^{-3} S/cm [3,4]. They have therefore been employed in multiple self-sensing applications for strain and temperature [15–22]. Many of these applications have been carried out free from conductive filler additives [17–21]. The change in electrical impedance of geopolymer substrates due to temperature and strain has been attributed to changes in ion migration [17,21] and percolation [19]. The former is a result of the quantum tunnelling effect in which at low external voltage the electrons are able to move to create a current. The latter is attributed to formation of a conductive passage in the material mainly with the use of conductive filler [43].

In general, sensing schemes apply a sinusoidal voltage of magnitude V and frequency f, to the sample and measure the current response, I. This allows the impedance to be calculated via [44]:

$$\vec{Z} = \frac{V}{I} e^{i(\phi_V - \phi_I)}, \tag{1}$$

where $\Phi_V - \Phi_I$ is the phase difference between the applied voltage and measured current and the impedance is a complex number of the form [44]:

$$\vec{Z} = Ze^{iarg(Z)}, \tag{2}$$

where Z and arg(Z) are the impedance's magnitude and argument. Geopolymers have a resistance (the real part of $\vec{Z}$ is non-zero) and a capacitance (the voltage lags the current, and the imaginary part of $\vec{Z}$ is negative). High frequency (f > 1 kHz) excitation is usually preferred over low frequency and dc for sensing, as it prevents electrolysis (the net migration of conductive Na^+ ions towards the cathode). Sensing schemes also typically employ a four-probe sensing method to reduce the effects of lead and contact resistances [45,46].

2.4 Temperature sensing

When using geopolymers as temperature sensors, it is often adequate to consider only the response of the impedance magnitude, Z, on temperature, T [47]:

$$\frac{Z}{Z_0} = e^{\left(\frac{a}{T} + bT + c\right)}, \tag{3}$$

where Z_0 is an arbitrary baseline impedance for normalisation, and a, b and c are characterised parameters which depend on geopolymer coating chemistry and geometry. An exponential decrease of impedance with temperature is expected as heat increases ionic mobility [16,18,48,49]. Equation (3) assumes that other measurands, such as water content and strain within the specimen are constant. If the temperature is high enough to cause significant water evaporation from the coating, for example, then the impedance of the specimen can increase due to water depletion [3,48].

2.5 3D printing of geopolymers

Recently, 3D printing has been introduced as a means of fabricating cementitious structures. Bypassing conventional moulds and formwork, cementitious materials can be extruded in a layer-by-layer process through a nozzle. Common additive manufacturing processes for curable pastes include contour crafting [50,51] and direct-ink writing [52–54].

Le et al. [55] introduced four properties that cementitious mixes should attain for 3D printing. Mixes and processes should exhibit adequate:

1. **Extrudability:** the ability of the mix to be extruded as a continuous filament from a dispensing unit.
2. **Buildability:** the number of layers that can be 'stacked' without any noticeable deformation, or the ability a material has to maintain its self-weight and the weight of subsequent layers[56].
3. **Workability or pumpability:** the ease with which the batch can move through a pumping system.
4. **Open time, or setting time:** the time window in which the mix remains extrudable.

Extrudability has also been referred to as 'printability' by Le et al. [55]. However, these two terms have recently developed separate meanings. While extrudability retains the original definition as the ability of a mix to be printed as a continuous filament, printability is regarded as something different. In particular it involves the interactions between the other properties in order to achieve a printable state [57–59].

Factors that affect the quality and performance of printed objects are speed, distance between nozzle and printer bed, nozzle size and shape, layer height, loading orientation and printing path [24,56,60–63].

Similar to OPC, geopolymer-based materials have already seen applications in 3D printing including the printing of fly ash and slag based mortars [23,58,64], glass fibre and steel cable reinforced mortars [24–26], one-part geopolymer mixes [27], metakaolin/fly ash lattices [53], kaolin/graphene composite suspensions [54] and powder-bed methods [61,65]. These previous studies have all mainly focused on the use of geopolymer 3D printing to produce bespoke construction elements. Additional applications include fly ash-based geopolymer foams for insulative applications [66] and kaolin-based geopolymers for electronic packaging [52]. Zhong et al. [67] have extruded electrically conductive geopolymer / graphene oxide composites, but the study focused on the printing of stand-alone objects (not coatings) and it was focused on demonstrating the effects of the graphene oxide additive volume fraction on dc conductivity.

The properties proposed by Le et al. [55] are a useful tool to guide the process of mix design and printing optimisation, but they are naturally subjective and application dependent. The application in this work, namely sensor-repair patches for concrete substrates, is inherently different to previous applications for 3D printed geopolymers. This meant that, mix development and fine turning was very much a process of optimisation, and had to exhibit two further properties. Geopolymers had to exhibit an adequate:

5. **Adhesion:** Defined by the pull-off strength of the geopolymer coating from the concrete substrate
6. **Electrical conductivity:** For a given electrode configuration, the geopolymer's electrical impedance should be measurable and allow for sensing.

For adhesion, one could view the concrete surface as an "old, previously printed layer" of deposited material, one that the newly deposited layer must adhere to. This highlights the challenge of achieving a high bond strength when using additive manufacturing, as it is known that increasing the time gap between layers has a negative effect on bond strength [55,56,60].

Note that electrical conductivity is a consideration of secondary importance, because the configuration of the electrodes and the electrical interrogation system can be modified to overcome any shortcomings in the conductivity of the material. However, these modifications do have a limit, and this imposes some limitations on the quantity and types of additives that can be added to the mix.

3. Methodology

3.1 Materials and mixing

In this work, kaolin sourced from the Southwest of England, UK, was calcined at 800 °C for 2 hours in an electric muffle furnace. The calcined clay was left to cool in the furnace prior to removing and storing in sealed containers. Silica fume was also added to the mix for greater densification [68]. The precursor consisted of 95% metakaolin and 5% silica fume. The properties of each material, provided by the supplier, are presented in Table 1.

Table 1 Material properties, including Brunauer–Emmett–Teller (BET) surface area.

	SiO_2	Al_2O_3	Mean particle size	BET surface area	Specific gravity
Kaolin	47 wt%	38 wt%	2 μm	14 m^2/g	2.6
Silica fume	90wt%	1 wt%	0.15 μm	-	-

The alkaline activator was made by combining sodium silicate (Na_2O = 8.5%, SiO_2 = 27.8%, H_2O = 63.7%) and 10 M sodium hydroxide solutions. The mass ratio of sodium silicate to sodium hydroxide was 2. After mixing, the solution was left to cool for at least 24h.

To improve adhesion by reducing shrinkage [9], 0.5 wt% PVA fibres (3 mm length) were added to the dry metakaolin precursor. The materials were dry mixed for 1 minute. The activator was then poured into the dry materials and mixed for 5 minutes until a homogenous mix was achieved. The precursor to solution ratio was 0.90. The amount and size of PVA fibres was based on the extrudability of the mix after a series of trial and error experiments explained in Section 4.

3.2 3D Printing overview

A screw cavity extruder fitted with a nozzle of size 18G (0.84 mm) was mounted onto a commercial 3D printer with an x-y gantry axis. A picture of the setup is presented in Figure 1. The steps in our 3D printing process were extended from [55] to encompass: 1) data preparation, 2) concrete surface preparation, 3) filament mixing and loading, 4) printing, 5) electrode insertion, and 6) curing. The printing process is outlined as a flowchart in Figure 2. It essentially explains the iterative process in 3D printing. Similar to other cement-printing flow charts, the data files are prepared by using a slicing software and the filament is prepared and printed [69]. As mentioned in Section 2.5 the mix must be extrudable and buildable. If the mix cannot be extruded, this signifies the need to reduce the mix's viscosity which is typically achieved by increasing liquid content, employing viscosity modifying agents and adjusting filler content [55,64]. Once the mix is extrudable, the mix is tested for buildability purposes as well. In like manner if buildability and shape retention are low, solid content is typically increased, more filler content is added and the viscosity is altered through the use of admixtures [53,64]. Compared to other flowcharts in 3D printing, the main differences are the addition of concrete surface preparation, electrode insertion and curing. In most cases these factors are absent, however in the current application these parameters must be investigated as they are paramount factors in ensuring proper function of sensing repairs. The printing process is explained in further detail in the Sections 3.2.1, Section 3.2.2 and Section 3.2.3.

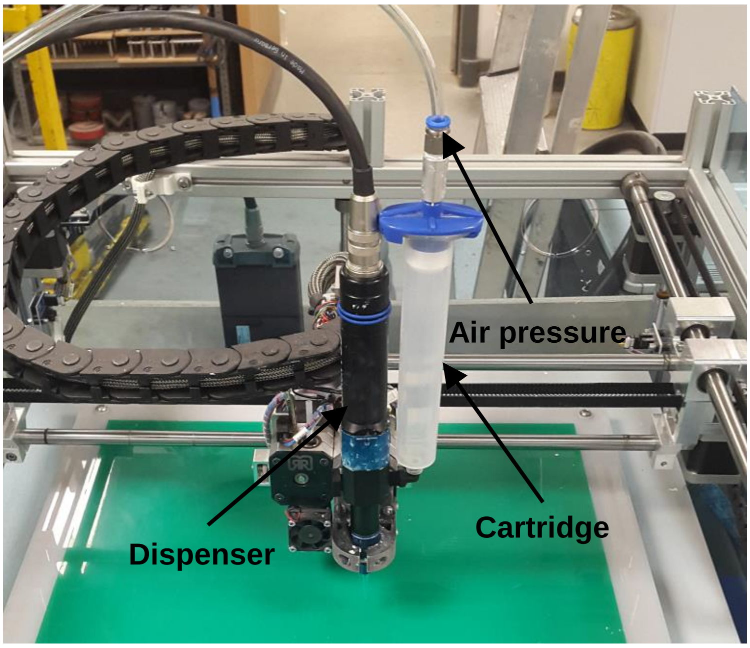

Figure 1: 3D printing setup showing the dispensing unit and an empty pressurized feed cartridge.

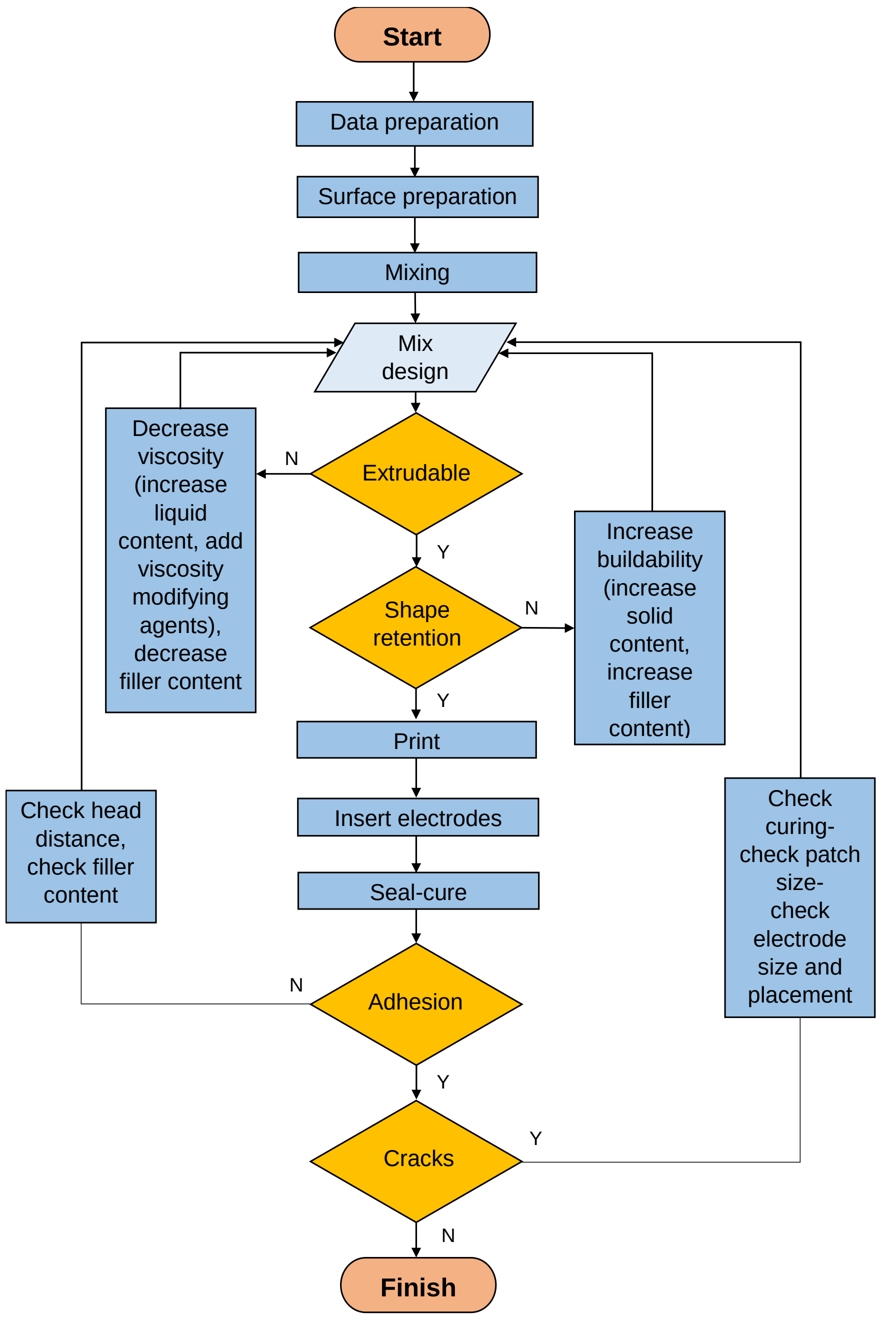

Figure 2: Flow chart of printing and fine-tuning process

3.2.1 Data preparation

A 3D CAD file of a double-layered patch was exported in stereolithography (STL) file format. Slicer software (Slic3r) was then used to generate G-Code from the STL, which defines the toolpaths for the printing head and stepper motor (extrusion) rates. Printing speeds were kept constant at 50 mm/s to avoid heterogeneities, a rectilinear density was chosen with 100% infill. A single perimeter was also added as the infill path can lead to gaps at the object's edges. Including a perimeter would close any potential gaps and allow greater interlocking of the extruded infill filament onto the outer shell [51]. The layer height was 0.66 mm. Figure 3 depicts an illustration of the sliced model.

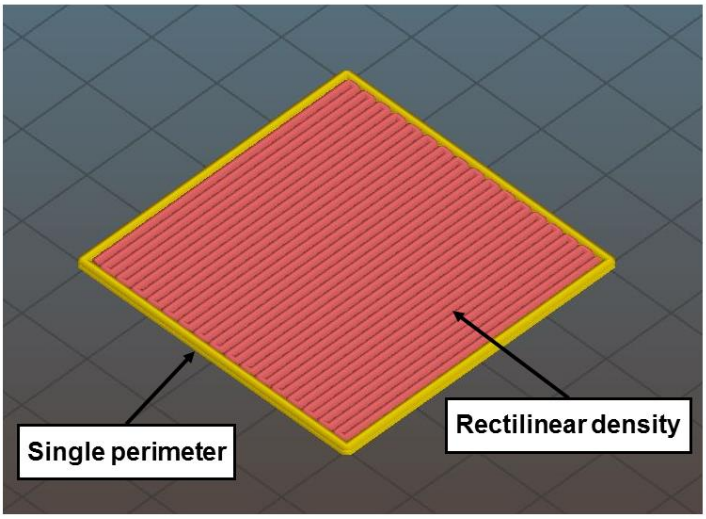

Figure 3: G-Code representation of patch

3.2.2 Concrete surface preparation

In this work, concrete slabs (70 mm x 20 mm x 20 mm) and cubes (side 100 mm) were printed onto. The top layer of the cube surface was removed with an electrical brush to expose the aggregates and improve adhesion between substrate and patch [40]. This is standard practice when repairing a concrete structure. In order to avoid liquid absorption, the concrete substrate was then pre-wetted [39] prior to printing to avoid excess liquid loss from the patch. The substrates were immersed in water at least for two hours and were removed shortly before printing. Excess water was removed with paper towels.

3.2.3 Filament mixing and loading

The geopolymer mix described in Section 3.1 was deposited into the barrel syringe (the cartridge labelled in Figure 1). As the material was, by design, not self-levelling, it was placed under an air pressure of 2 bar to force the material to flow into the screw extruder's dispensing cavity. Figure 4a presents a drawing of the dispensing unit printing and Figure 4b depicts a photograph of the printing procedure on a concrete slab. The density of the mix was 1.73 g/mL and the flowrate of the mix during printing was 2 mL/min.

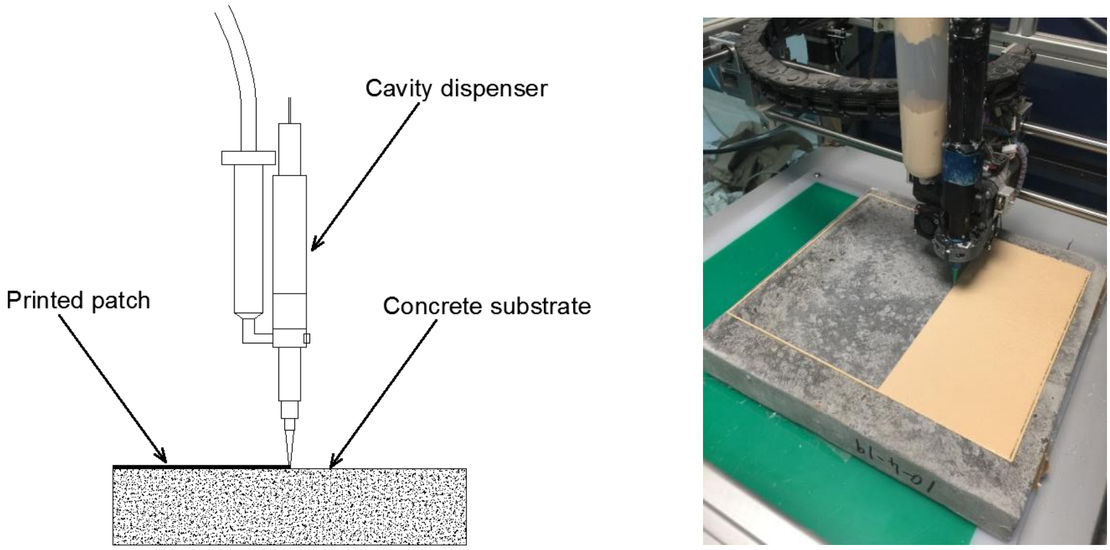

(a) (b)

Figure 4: a) Schematic diagram and b) photograph of geopolymer being extruded onto concrete slab.

3.2.4 Electrode insertion

The probes for electrical sensing attached were stainless steel wires, attached according to the Van Der Pauw (VDP) configuration [70] in order to minimize the electrode effect on the integrity of the patch. The VDP configuration also provides an average (rather than localised) measurement of the patch's overall impedance. Two methods of incorporating the electrodes were tested in this work:

- Method 1: was to pre-arrange the probes on the concrete substrate and print directly over them.
- Method 2: probes were inserted into the patch after the patch was printed.

3.2.5 Curing

The samples were then stored in sealed, plastic containers to maintain moisture and cured at 40 °C for 24 hours. The elevated temperature is not mandatory [13] but accelerates the geopolymerization process. The samples were then kept under ambient conditions until testing.

3.3 Sensor testing

The electrical properties of the patch were analysed with an electrical impedance analyser running in potentiostatic mode. The impedance of the samples was measured by applying 10 mV voltage for frequencies between 10 Hz and 0.5 MHz and measuring the electrical current response. The impedance was then determined using equations (1) and (2) listed in Section 2.3. The electrical configuration is depicted in Figure 5. The voltage was applied across electrodes 1 and 4 and the current was measured across electrodes 2 and 3.

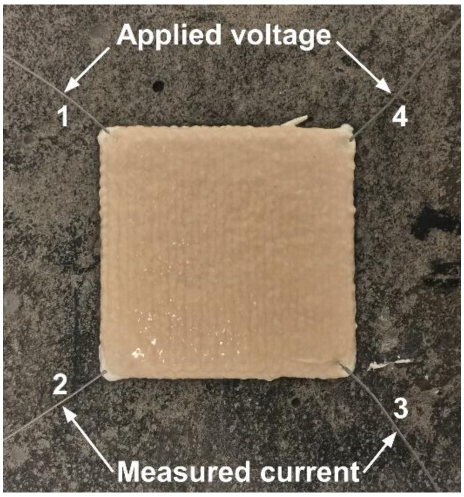

Figure 5: Printed sensor on a concrete substrate

In order to avoid humidity fluctuations during temperature experiments, samples were placed in a controlled environmental chamber. The chamber set the temperature at 30 °C and then reduced it to 10 °C in 5 °C steps: we denote this the "down cycle". It then performed an "up cycle", increasing temperatures from 10 °C to 30 °C in 5 °C steps. When target temperatures were reached, they were held for 135 minutes to ensure thermal stabilisation of the patch and the concrete substrate. Following this, temperatures were held for a further 15 minutes and measurements of impedance were taken. This allowed for extraction of average values of impedance components over this time period. Note that this long measurement period is not something that would be required during sensor operation, but it does improve measurement confidence during characterisation. The temperature steps as recorded by an external sensor are presented in Figure 6.

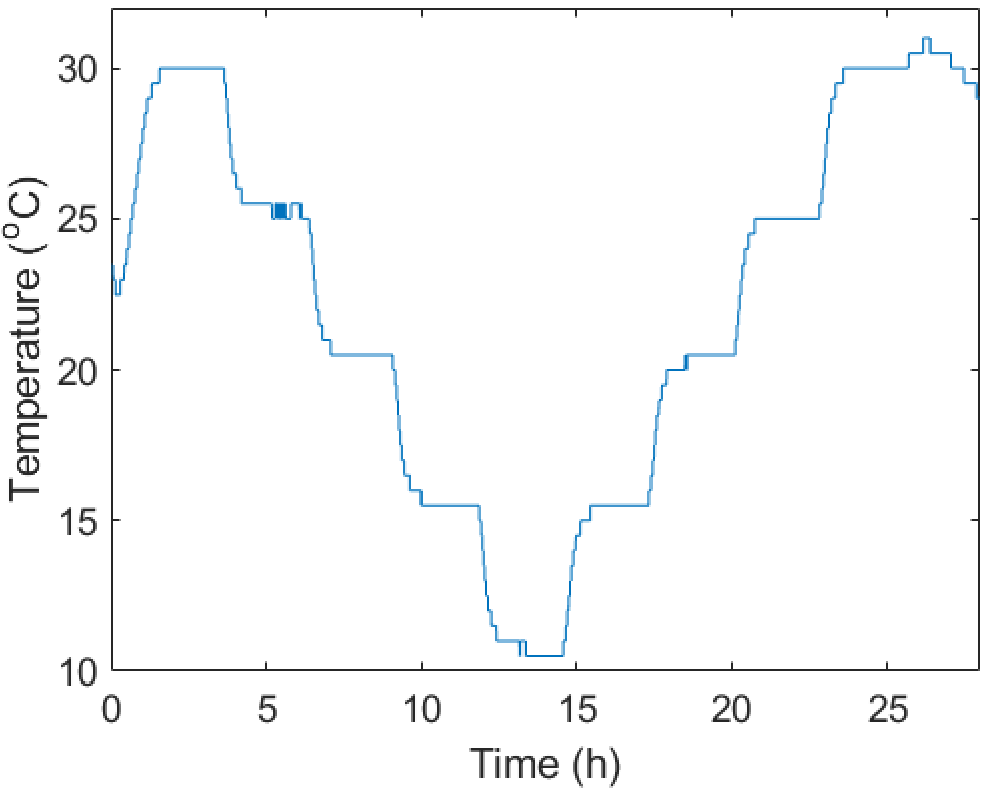

Figure 6: Time-temperature series for temperature characterization.

3.4 Mechanical properties

3.4.1 Compressive strength

As there was more focus on achieving an adequate adhesion with the concrete layer, the mix's buildability was not sufficient enough to print specimens for compression testing. For this reason, the compressive strength of the batch was tested for casted samples rather than printed ones. After mixing, the geopolymer paste was placed into six silicon moulds 30 mm x 30 mm x 25 mm and vibrated for 10 minutes to remove the entrapped air. Each mould was then wrapped with plastic film, sealed in a plastic container and cured at 40 ^{o}C for 24 hours. The samples were left to cure in an environmental chamber for another 27 days at 20 ^{o}C until testing. The compressive strength was measured with a universal loading cell at a loading rate of 0.5 mm/s.

3.4.2 Adhesion testing

The bond strength of printing repair patches was evaluated by using a pull-off adhesion tester in accordance to standard BS EN 1542-1999 [71]. In order to avoid shrinkage issues and allow for quicker curing as discussed further below in Section 4.4, double layered 90 mmx 90 mm patches were printed on separate 100 mm cubes instead of a slab. This was to allow for quick sealing for each specimen to avoid liquid evaporation. Five samples were tested 6 days after extrusion. Figure 7a and 7b depict a schematic drawing and a picture of the cored samples. As per BS EN 1542-1999:

- The samples were core drilled with a 50 mm diameter cylinder through the repair product and into the concrete substrate (total depth 10 mm).
- Following this, an epoxy adhesive was used to attach an aluminium 50 mm dolly to the cored surface. The centre of the dolly was aligned with the centre of the core to limit eccentricity issues and assure proper load application.
- The epoxy was left to dry as per manufacturer requirements. The adhesion tester (Elcometer) was then fastened onto the dolly for pull-off testing. The nut of the tester was tightened to evenly apply force to the dolly and subsequently stress to the coating. The nut was tightened until the dolly was removed from the substrate and a reading was taken for each sample.

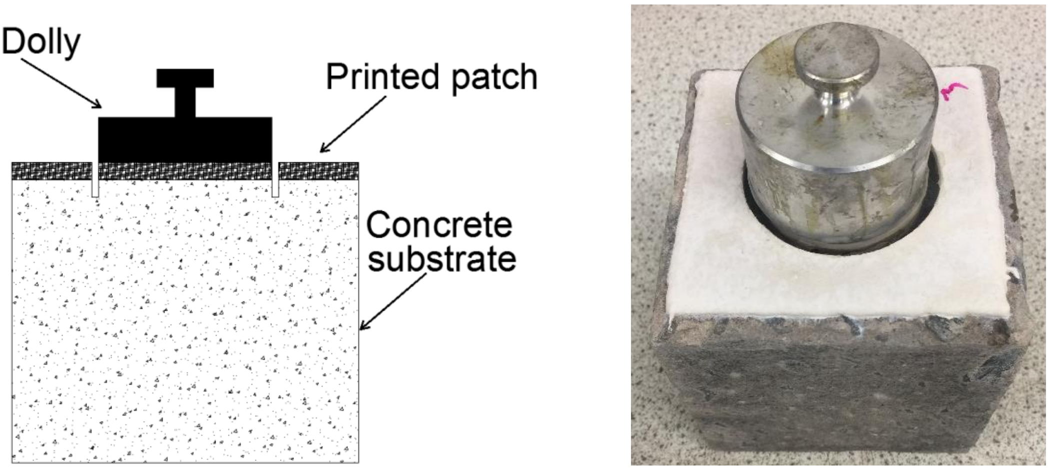

(a) (b)

Figure 7: Printed overlay for adhesion test a) schematic drawing of sample b) picture of sample

4. 3D printing: tuning and improvement

4.1 Baseline properties

This section briefly outlines some of the challenges overcome in developing the mix design and printing process outlined in Section 3. We began by qualitatively addressing three of Le et al's [55] baseline properties for 3D printing, as outlined in Section 2.5:

1) Extrudability: Once the precursor and alkaline solution are mixed together, the gel phase of geopolymerisation commences [30]. The homogeneous and cohesive nature of the gel makes achieving printable mixes relatively straightforward. The extrudability of the mix was tested by extruding three straight lines 4 mm apart. If the lines retained their intended shaped and were free from gaps the mix was deemed extrudable. Figure 8 displays the printed lines for the mix described in Section 3.1.

Figure 8: Extrudability test showing three printed lines of material.

2) Pumpability/workability: Pumpability/workability is particularly important to consider for syringe-based 3D printers [52–54,58] or when materials must be conveyed long distances to the nozzle. In this work, we were able to design out stringent pumpability requirements by using a local cartridge of material fed to a progressive cavity (screw) extruder, which can pump low and high viscosity fluids at stable rates. This was required in this work because metakaolin geopolymers can present workability and mixing issues due to their large liquid demand [32].

4) Open time: The open time of the mix was investigated as a continuation of extrudability. It was found that the mix was able to be extruded without any gaps for about 60 minutes at ambient temperatures, as a consequence of the water content in the alkaline solution [72]. This was a long enough duration to deposit around 100 mL of material (several full cartridges). It should be noted though, that this is not the setting time of the paste associated with a Vicat needle test. During printing the paste can eventually congeal inside the dispenser due to heat generation from friction as the screw rotates disrupting the flow thus leading to extrusion issues.

4.2 The buildability adhesion trade-off

The final requirement, and the one that required the most mix design alterations was the trade-off between buildability and adhesion (and to a lesser extent, a trade-off with electrical conductivity) mentioned in Section 2.5. Unfortunately, in cementitious materials, a high buildability and high adhesion tend to be two contradictory requirements. Normally, buildability of a cementitious material (including geopolymer) would be increased by increasing its solid content [73], but this comes at the expense of inter-layer and substrate adhesion [56,63,74,75], higher shrinkage due to greater stress development [76] and conductivity [4,77], as shown in Table 2. In other words, opting to maximize the patch's printing potential would compromise the repair and sensing aspects of the patch. For this reason, a zero-slump mix was not suitable for this sort of application.

Table 2 Functional requirements for 3D printed self-sensing materials

	3D printing/extrusion	Repairs	Self-sensing materials
Solid content	High	Low (high liquid content)	High liquid content (greater conductivity)
Surface quality	Smooth flat surface	Rough surface better adhesion	-

This issue could be solved by using several mixes, such as a low viscosity primer layer followed by more viscous additional layers for printing. This would come at the cost of process complexity and cost. In this case, we were able to find an optimal mix by sacrificing some buildability. A solid-liquid ratio of 0.9 allowed the geopolymer to maintain shape stability, and provide reasonable adhesion (see

Section 5). For this application, sacrificing buildability for adhesion was worthwhile, as we only needed to print coatings which were a few layers thick. Any thicker, and we would risk debonding of the coating during curing due to shrinkage, as outlined in Section 2.2.

4.3 The concrete substrate

Another matter to consider is the 'printing bed' in these applications. Normally a flat surface is required to ensure proper structural integrity and avoid deformations in subsequent layers [62]. The effective printing bed in this application is the concrete substrate.

For repairs a rough surface is preferred to ensure proper adhesion and interlocking between repair and substrate [39]. However, this could pose various issues in printing especially when small nozzle sizes are employed. Firstly, this could result to nozzle obstruction if proper head distance (distance between substrate and nozzle) is not considered. Secondly, if a large head distance is selected to avoid any potential interferences, the unevenly distributed surface can result in a printed object with ununiform quality. Figures 9a and 9b present an example of such an effect. It could be viewed that the area with a higher head distance resulted in poorer quality and gaps in printing in comparison to the area with a shorter head distance. The higher distance prevented proper interlocking with the substrate, which led to dragging of the filament and inaccurate deposition creating a mismatch between previous and subsequent printing paths.

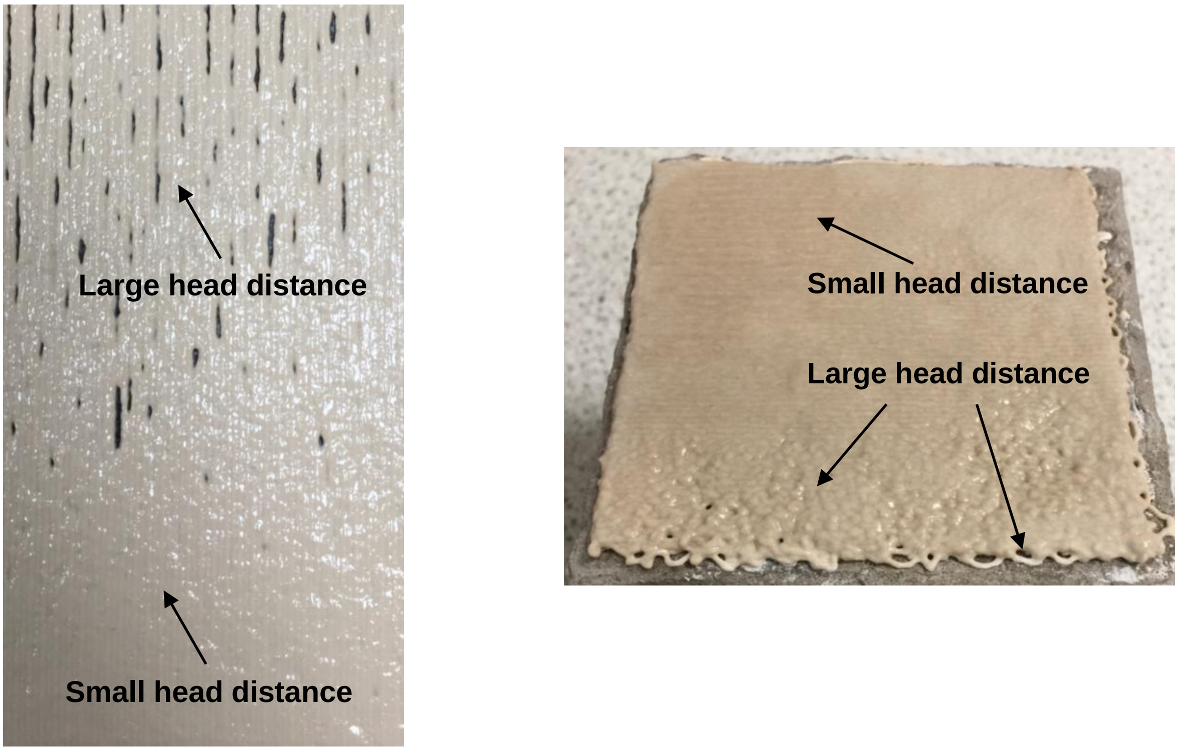

(a) (b)

Figure 9: Examples of adverse print quality due to uneven concrete surface and head distance

4.4 Shrinkage control

Shrinkage in this system is a vital point of consideration and thus proper shrinkage control is required to avoid the formation of cracks. Tensile stresses develop between the substrate and the repair which could result into cracks [34]. Moreover, metakaolin based repairs are prone to delamination [78] and cracks [36] primarily due to high levels of shrinkage. For this reason, incorporating additives to deal with these issues is necessary. PP [12,35] and PVA [9] fibres could provide a solution to high restrained shrinkage. Water loss in the system is also an issue to tackle. Pre-wetting the substrate prevents loss of liquid in the patch [39]. Figure 10 presents a square patch printed onto a dry substrate. Furthermore, sealing the sample prevents water evaporation during thermal curing [79]. It should be added that thermally curing also leads to reduced cracks and increased bond strength [9].

Figure 10: Cracked patch printed onto dry concrete substrate

In order to counter shrinkage issues, the use of fibre additives was employed. However, having tested PP fibres, extrudability was found to be poor even at 0.5-1% w/w, as the inflexible fibres would cluster near the nozzle and cause congestion. Short (3 mm) PVA fibres, being more flexible, did not cause extrudability issues at 0.5 % w/w (6 mm fibres compromised extrudability). The inclusion of PVA fibres enhances shape stability [57]. In addition, according to Zanotti et al. [9], PVA fibres also increase the bond strength of repairs, as they decrease repair cracking and delamination due to restrained shrinkage, and enhance interfacial failure resistance with the patch and the concrete substrate. The fibres are able to bridge the gaps of cracks while carrying the induced tensile loads [80].

Another factor that may be overlooked for shrinkage control when printing overlays for repairing purposes is the total print time. Rapid drying can occur when large surface areas are being repaired with relatively thin overlays. This relevant in 3D printing applications especially when the extrusion rate is low. This can subsequently prolong the total print run and delay proper curing leading to potential moisture loss. [81]. The repair application must be quick enough to avoid material hardening and developing high viscosity. Low viscosity is desired as it would be able to spread on the surface and enable penetration into the capillaries [75]. In order to accomplish this in the current application, increasing the print speed was an option. However, as could be seen in Figures 11a and Figure 11b, increasing print speed from 50mm/s to 100mm/s had a negative impact on the quality of the print leading to multiple gaps and thus poor printing. This is mainly because the volume of material that can be extruded per second (and therefore per mm) is limited in our set up.

Taking everything into account when extruding for repairing purposes the printing duration, speed and any delays, should be such that does not negatively impact the repair quality but at the same time is quick enough to maintain adequate viscosity and to allow proper sealing and curing to avoid moisture loss. In essence, the open time in repair applications can be viewed as not by the time a mix is printable but in which the time a mix can achieve adequate adhesion while avoiding excessive shrinkage. This, however, is closely linked to equipment limitations which can cause variations in the final time.

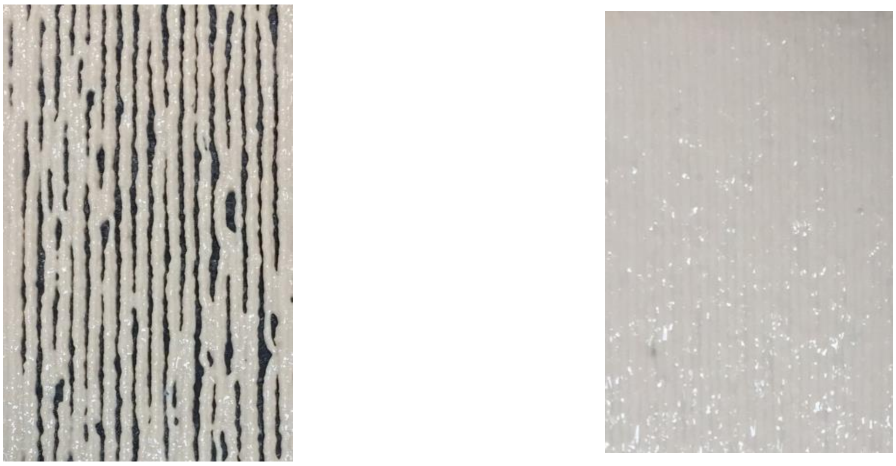

100 mm/s　　　　50 mm/s

(a)　　　　(b)

Figure 11: Poor printing due to increased print speed: a) printing at 100 mm/s, and b) printing at 50 mm/s.

4.5 Electrode insertion

Electrode insertion is another parameter to take into account when 3D printing self-sensing materials. In conventional smart materials, embedded electrodes are often inserted into moulds prior to casting to ensure proper placement [82]. However, as 3D printing is a means of fabrication without the use of moulds, other routes must be considered. In general, electrodes alone are capable of generating cracks in cementitious materials [83]. Therefore, a proper electrode insertion method is necessary to avoid any addition impairments to the patches. Figures 12a and 12b present the two electrode insertion methods outlined in Section 3.2.4. Figure 12a refers to method I in which the electrodes are prearranged and printed directly over and Figure 12b depicts method II in which the electrodes were inserted into the object after it was printed.

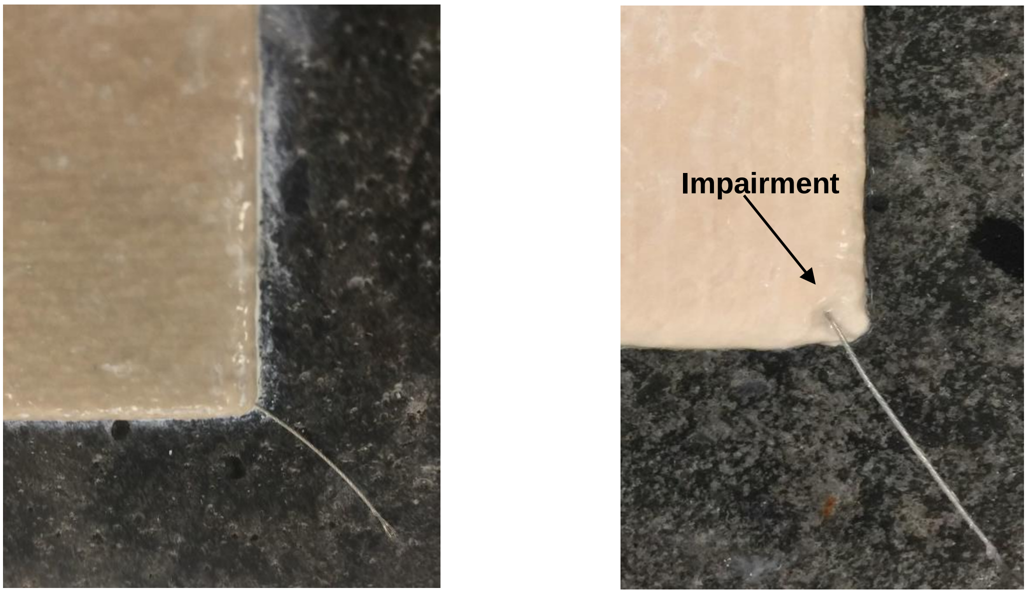

Method I　　　　Method II

(a)　　　　(b)

Figure 12: Electrode insertion methods can be a) prearranged, or b) inserted after printing.

It is evident that inserting the electrodes after printing causes impairments to the printed object compared to printing directly onto them in a prearranged manner. When using method II the patch is still in a relatively fresh state and it is still susceptible to deformations. Any unaccounted interferences can impair the shape of the printed object, which in turn will carry over to the hardened state of the material. This could pose an issue as this practice could generate undesired cavities making it prone to water and chloride ingress. Furthermore, depending on the electrode size and impairment caused, the geometrical and mechanical properties of the patch could be affected, and this can have knock-on effects on sensor performance and reliability.

5. Results and discussion

5.1 Printed sensor: impedance response to temperature

Figure 13a present a typical Nyquist plot for a printed patch at room temperature (20 °C), for frequencies between 10 Hz and 0.5 MHz respectively. As can be seen, the Nyquist plot of the patch differs from the traditional semi-circle Nyquist plot of a geopolymer cube as depicted in Figure 13b which is expected in cementitious materials [84]. The difference in Nyquist plots can be attributed to various factors most likely influenced by the concrete-geopolymer interaction. The positive calcium ions (Ca^{2+}) from the concrete charge-balance the negative charge due to the aluminium (Al^{3+}) ions in the geopolymer creating a chemical bond at the interface between these two materials [33]. The material that is being measured is the metakaolin geopolymer coating which is inherently low on calcium (Ca) content [29]. It could be speculated that the chemical bond developed at the interface between concrete and geopolymer results into a non-homogenous area compared to the rest of the coating affecting the electrical properties at lower frequencies, introducing more than one semi-circle [85]. Similar behaviour can be observed in concrete-steel interfaces in which the typical semi-circle cannot be employed in that configuration due to the interaction between steel and concrete [85,86]. The magnitude of the impedance, Z, was relatively stable for each measurement between 10-1000 Hz with a slight decreasing tendency that was more evident beyond 1000 Hz. Bearing this in mind, we can infer that frequency has a minor effect on the sensing capacity of the patch.

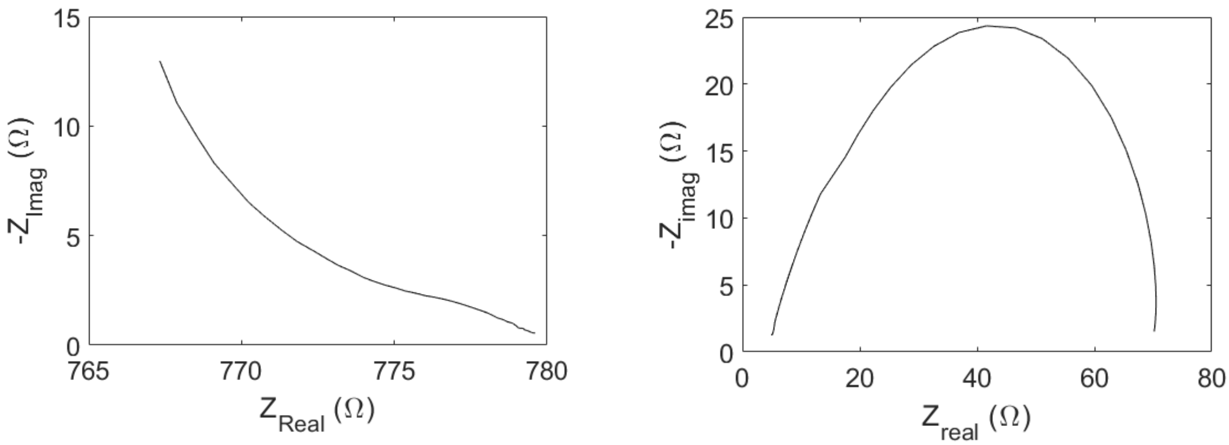

(a) (b)

Figure 13: a) Typical Nyuist plot of printed patch. b) Typical Nyuist plot of metakaolin geopolymer cube

Figures 14 and 15 depict the Nyquist and Bode plot respectively for frequencies between 10 Hz – 10^5 Hz for the down cycle. As shown, a clear shift in impedance can be observed for the different temperatures in both the Nyquist and Bode plot for each cycle. The sensor's response is in accordance to the expected behaviour of geopolymers under these circumstances. In specific, the impedance decreased with increasing temperature and increased when the temperature decreased. The change in impedance under these conditions can be attributed to ion mobility in the pores of the patch. This behaviour is in accordance to previous authors [16,18,48].

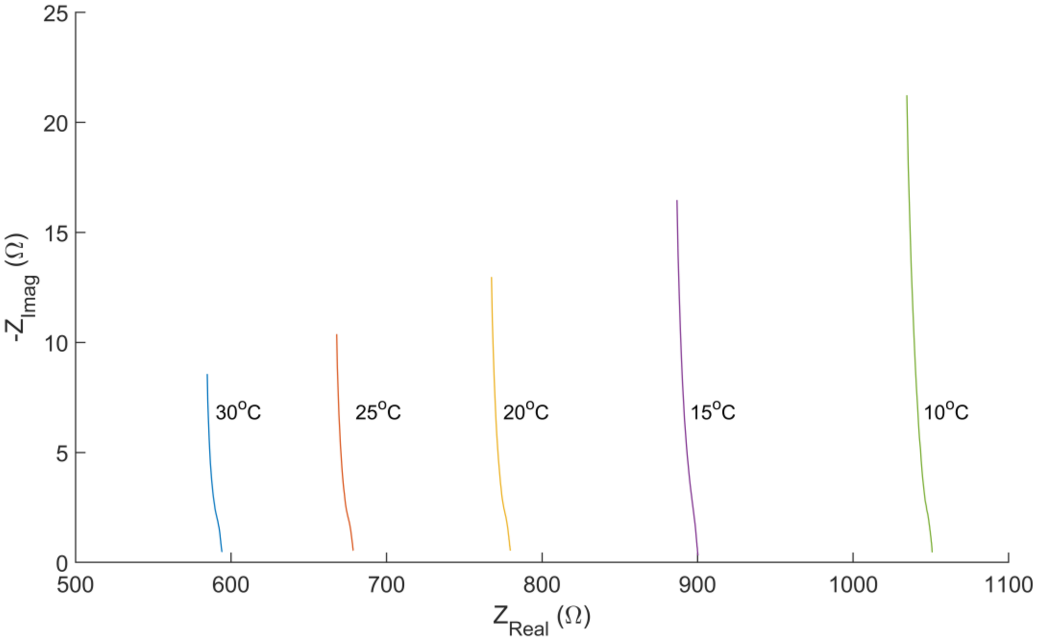

Figure 14: Nyquist plot for each temperature during a down cycle

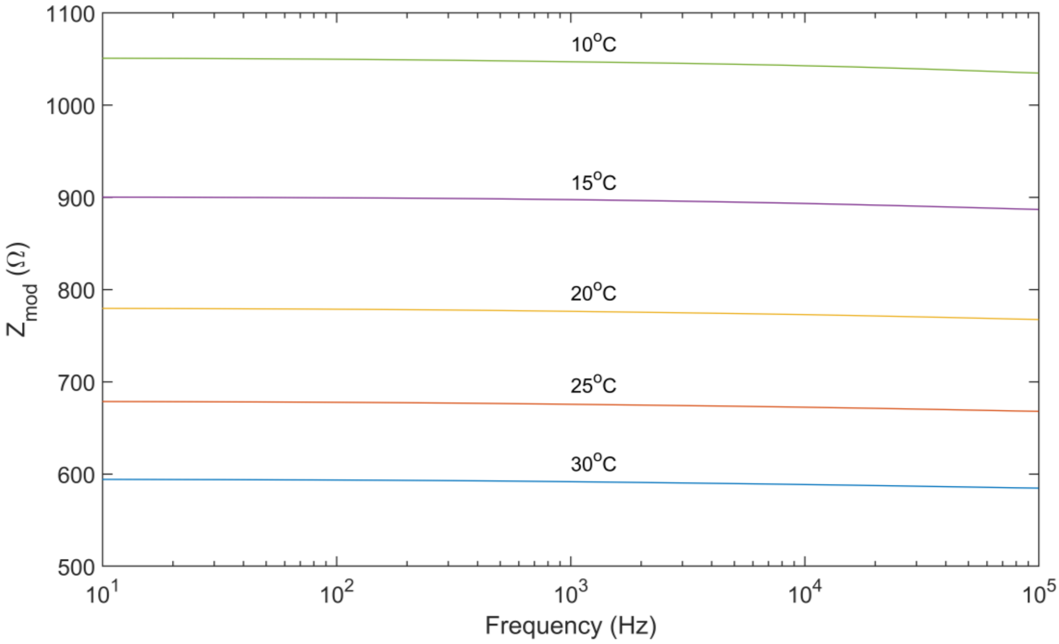

Figure 15: Bode plot for each of temperature during a down cycle

Figure 16 plots the sensor response (at 1 kHz) against temperature during two temperature cycles taken over two days. The fit to equation (4) is excllent, and the sensor response is repetable: the pooled repeatability was measured to be 0.3 °C. Under the current experimental conditions it has been assumed that the moisture content in the patch is relatively stable as moisture is controlled due to sealed conditions and under the assumption no liquid in the patch is lost due absorption from the concrete substrate. In practice, moisture conditions can be compensated for with a reference sensor.

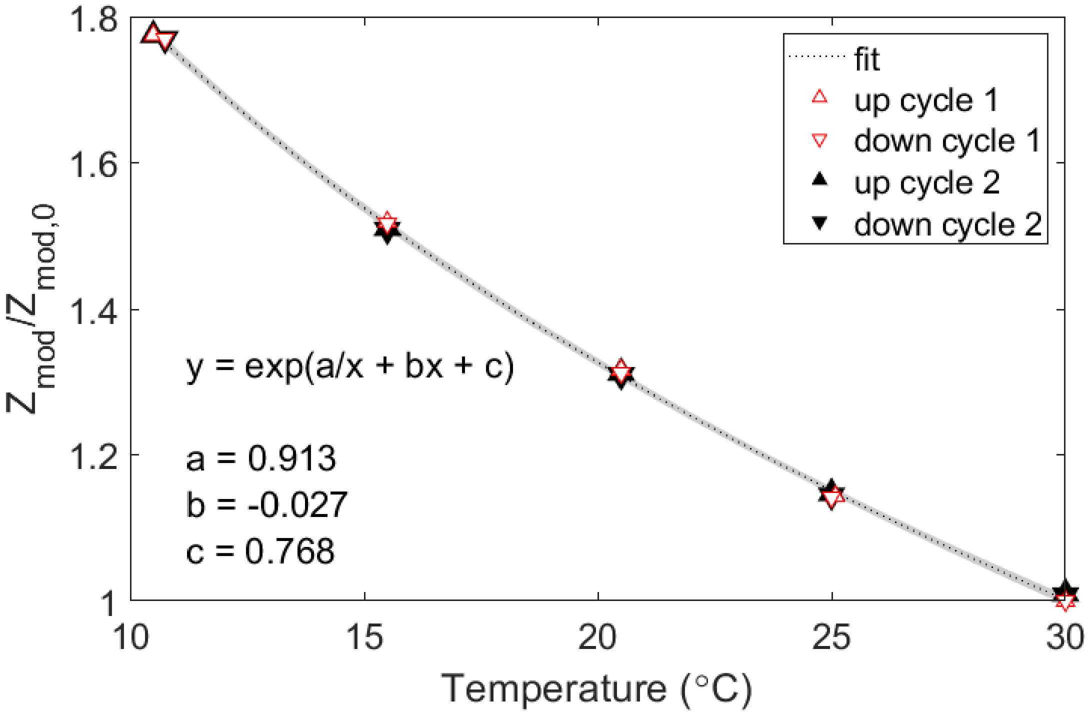

Figure 16: Normalised impedance response of geopolymer patch to temperature during four temperature cycles. Shaded regions shows the 95% confidence interval of the fit

5.1.1 Compressive strength

The compressive strength of the mix was 24 ± 1.7 MPa after 1 day. This is slightly lower than a typical geopolymer mix, and this is likely due to the high water content in the extrudable mix: this is considered to hinder high strength development of the geopolymer [87].

5.1.2 Adhesion results

The average bond strength between the printed patch and the concrete substrate for 5 samples was 0.6 ±0.16 MPa. The failure type in all geopolymer overlays was adhesion failure (failure at the interface between the substrate and the repair). Conventionally applied metakaolin-based repairs with proper optimization can achieve adhesion strength within the range of 1 - 2 MPa with the pull-off test [14,78]. The difference in strength can be attributed to numerous factors. Firstly, as shown by Vasconcelos et al. [36], metakaolin based geopolymer repairs can achieve poor bonding performance if the mix design is not properly tailored. Metakaolin geopolymers have a high liquid demand, which leads to excessive water in the alkaline solution. This promotes drying shrinkage thus compromising the bond between the repair and the substrate at the interface [9,78]. Furthermore, the low adhesion strength can also be attributed to 3D printing fabrication process. It could be that the mix is not coming in to full contact with the substrate, thus compromising anchorage between the two materials [75]. While the geopolymer repair was tuned to achieve both adequate printability and adhesion in this experiment, the mix design was not optimized for achieving maximum levels of bond strength, due to the trade-offs discussed in Section 4.2.

Another crucial factor that needs to be taken into account is the concrete substrate. In typical 3D printing applications, the printing bed should be level and smooth to ensure proper stability during printing. In the current application, the effective printing bed is the concrete substrate, which as previously mentioned in Section 3.2.2, has a rough surface to promote greater adhesion between the repair and the substrate. While this practice is meant to increase adhesion, it could simultaneously compromise adhesion in extrusion applications. As the head distance is measured from the highest peak of the surface in order to avoid nozzle obstruction, apart from gaps in printing as mentioned in Section 4.4, the contact between the two materials will not be uniform. This issue is even more prevalent the rougher the surface is. As illustrated in Figure 17 the geopolymer filament may not come into full contact with the substrate when the material is deposited onto a valley (area between two peaks on the surface). This could result into air pockets in the repair and due to the lack of compaction in the extrusion process this could cause an adverse effect on its bonding performance [88].

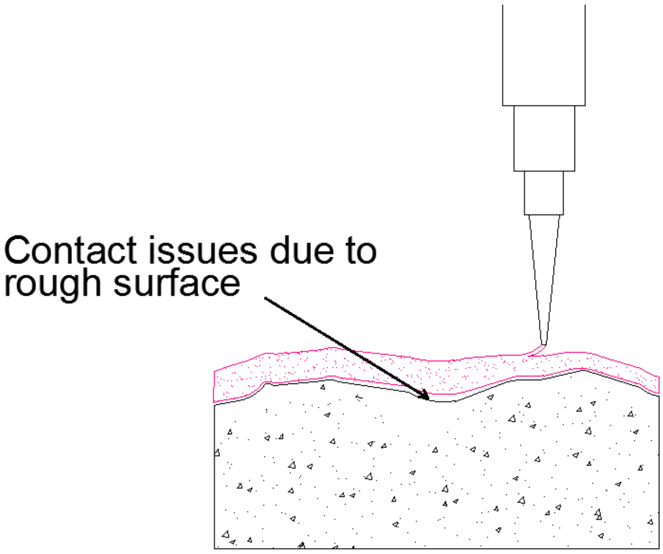

Figure 17: Non-uniform contact due to the rough surface of the concrete substrate

A potential solution to work around rough surfaces would be to employ a nozzle with a diameter larger than to the height difference between the highest and lowest peak of the surface to avoid the formation of air pockets. Moreover, this allows greater surface coverage which would minimize layers and print paths thus lessening the formation of gaps in the material formed due to printing and subsequently leading to a stronger object [50,89]. In addition, setting a smaller layer height than the nozzle diameter allows for greater compaction between layers [62] which could enable greater contact between the patch and the substrate. Finally, digitally scanning the surface profile and creating a respective G-code file could properly tailor the repair to the respective substrate. Further investigation is required to optimize the mix design and printing process to allow for a more suitable repair solution.

6. Conclusions

In this paper a 3D printed, multifunctional geopolymer sensor-repair for concrete structures was presented. The fabrication process and the temperature sensing response of the printed sensor were outlined. The performance of the sensor was in accordance to the expected behaviour of geopolymer dependence to temperature, with a resolution of 0.1 °C and a repeatability of 0.3 °C. The adhesion of the printed patch to the concrete substrate was 0.6 MPa. This bond strength was lower than a typical geopolymer repair due to the high degree of drying shrinkage and limitations in the 3D printing process itself. Further investigation is required to optimize 3D printing for repair and sensing applications. Future work involves exploring the sensor's capability in other areas such as strain sensing and damage detection.

Acknowledgments

The authors would like to thank Brenden Lavoie from the University of Toronto for assisting in the computer-aided design of the printing setup.

Funding

This work was supported in part by the Royal Society (grant number RG160748), and the Oil & Gas Innovation Centre (OGIC).

References

[1] J.L. Provis, Alkali-activated materials, Cem. Concr. Res. 114 (2018) 40–48. https://doi.org/10.1016/j.cemconres.2017.02.009.

[2] J.L. Provis, S.A. Bernal, Geopolymers and Related Alkali-Activated Materials, Annu. Rev. Mater. Res. 44 (2014) 299–327. https://doi.org/10.1146/annurev-matsci-070813-113515.

[3] X.M. Cui, G.J. Zheng, Y.C. Han, F. Su, J. Zhou, A study on electrical conductivity of chemosynthetic Al2O3-2SiO2geoploymer materials, J. Power Sources. 184 (2008) 652–656. https://doi.org/10.1016/j.jpowsour.2008.03.021.

[4] S. Hanjitsuwan, P. Chindaprasirt, K. Pimraksa, Electrical conductivity and dielectric property of fly ash geopolymer pastes, Int. J. Miner. Metall. Mater. 18 (2011) 94–99. https://doi.org/10.1007/s12613-011-0406-0.

[5] R. Pouhet, M. Cyr, Formulation and performance of flash metakaolin geopolymer concretes, Constr. Build. Mater. 120 (2016) 150–160. https://doi.org/10.1016/j.conbuildmat.2016.05.061.

[6] P. Nath, P.K. Sarker, Flexural strength and elastic modulus of ambient-cured blended low-calcium fly ash geopolymer concrete, Constr. Build. Mater. 130 (2017) 22–31. https://doi.org/10.1016/j.conbuildmat.2016.11.034.

[7] F.U.A. Shaikh, Mechanical and durability properties of fly ash geopolymer concrete containing recycled coarse aggregates, Int. J. Sustain. Built Environ. 5 (2016) 277–287. https://doi.org/10.1016/j.ijsbe.2016.05.009.

[8] F.N. Okoye, S. Prakash, N.B. Singh, Durability of fly ash based geopolymer concrete in the presence of silica fume, J. Clean. Prod. 149 (2017) 1062–1067. https://doi.org/10.1016/j.jclepro.2017.02.176.

[9] C. Zanotti, P.H.R. Borges, A. Bhutta, N. Banthia, Bond strength between concrete substrate and metakaolin geopolymer repair mortar: Effect of curing regime and PVA fiber reinforcement, Cem. Concr. Compos. 80 (2017) 307–316. https://doi.org/10.1016/j.cemconcomp.2016.12.014.

[10] K. Sakkas, D. Panias, P.P. Nomikos, A.I. Sofianos, Potassium based geopolymer for passive fire protection of concrete tunnels linings, Tunn. Undergr. Sp. Technol. 43 (2014) 148–156. https://doi.org/10.1016/j.tust.2014.05.003.

[11] R. Robayo-Salazar, C. Jesús, R. Mejía de Gutiérrez, F. Pacheco-Torgal, Alkali-activated binary mortar based on natural volcanic pozzolan for repair applications, J. Build. Eng. 25 (2019) 100785. https://doi.org/10.1016/j.jobe.2019.100785.

[12] A.M. Aguirre-Guerrero, R.A. Robayo-Salazar, R.M. de Gutiérrez, A novel geopolymer application: Coatings to protect reinforced concrete against corrosion, Appl. Clay Sci. 135 (2017) 437–446. https://doi.org/10.1016/j.clay.2016.10.029.

[13] L. Biondi, M. Perry, C. Vlachakis, Z. Wu, A. Hamilton, J. McAlorum, Ambient Cured Fly Ash Geopolymer Coatings for Concrete, Materials (Basel). 12 (2019) 923. https://doi.org/10.3390/ma12060923.

[14] S. Kramar, A. Šajna, V. Ducman, Assessment of alkali activated mortars based on different precursors with regard to their suitability for concrete repair, Constr. Build. Mater. 124 (2016) 937–944. https://doi.org/10.1016/j.conbuildmat.2016.08.018.

[15] M. Saafi, L. Tang, J. Fung, M. Rahman, F. Sillars, J. Liggat, X. Zhou, Graphene/fly ash geopolymeric composites as self-sensing structural materials, Smart Mater. Struct. 23 (2014).

https://doi.org/10.1088/0964-1726/23/6/065006.

[16] M. Saafi, G. Piukovics, J. Ye, Hybrid graphene/geopolymeric cement as a superionic conductor for structural health monitoring applications, Smart Mater. Struct. 25 (2016). https://doi.org/10.1088/0964-1726/25/10/105018.

[17] M. Saafi, A. Gullane, B. Huang, H. Sadeghi, J. Ye, F. Sadeghi, Inherently multifunctional geopolymeric cementitious composite as electrical energy storage and self-sensing structural material, Compos. Struct. 201 (2018) 766–778. https://doi.org/10.1016/j.compstruct.2018.06.101.

[18] M. Perry, M. Saafi, G. Fusiek, P. Niewczas, Hybrid optical-fibre/geopolymer sensors for structural health monitoring of concrete structures, Smart Mater. Struct. 24 (2015). https://doi.org/10.1088/0964-1726/24/4/045011.

[19] C. Lamuta, L. Bruno, S. Candamano, L. Pagnotta, Piezoresistive characterization of graphene/metakaolin based geopolymeric mortar composites, MRS Adv. 2 (2017) 3773–3779. https://doi.org/10.1557/adv.2017.595.

[20] P. Rovnaník, I. Kusák, P. Bayer, P. Schmid, L. Fiala, Comparison of electrical and self-sensing properties of Portland cement and alkali-activated slag mortars, Cem. Concr. Res. 118 (2019) 84–91. https://doi.org/10.1016/j.cemconres.2019.02.009.

[21] S. Bi, M. Liu, J. Shen, X.M. Hu, L. Zhang, Ultrahigh Self-Sensing Performance of Geopolymer Nanocomposites via Unique Interface Engineering, ACS Appl. Mater. Interfaces. 9 (2017) 12851–12858. https://doi.org/10.1021/acsami.7b00419.

[22] L. Deng, Y. Ma, J. Hu, S. Yin, X. Ouyang, J. Fu, A. Liu, Z. Zhang, Preparation and piezoresistive properties of carbon fiber-reinforced alkali-activated fly ash/slag mortar, Constr. Build. Mater. 222 (2019) 738–749. https://doi.org/10.1016/j.conbuildmat.2019.06.134.

[23] B. Panda, S.C. Paul, L.J. Hui, Y.W.D. Tay, M.J. Tan, Additive manufacturing of geopolymer for sustainable built environment, J. Clean. Prod. 167 (2017) 281–288. https://doi.org/10.1016/j.jclepro.2017.08.165.

[24] B. Panda, S. Chandra Paul, M. Jen Tan, Anisotropic mechanical performance of 3D printed fiber reinforced sustainable construction material, Mater. Lett. 209 (2017) 146–149. https://doi.org/10.1016/j.matlet.2017.07.123.

[25] J.H. Lim, B. Panda, Q.C. Pham, Improving flexural characteristics of 3D printed geopolymer composites with in-process steel cable reinforcement, Constr. Build. Mater. 178 (2018) 32–41. https://doi.org/10.1016/j.conbuildmat.2018.05.010.

[26] G. Ma, Z. Li, L. Wang, G. Bai, Micro-cable Reinforced Geopolymer Composite for Extrusion-based 3D Printing, Mater. Lett. 235 (2019) 144–147. https://doi.org/10.1016/j.matlet.2018.09.159.

[27] B. Panda, G.B. Singh, C. Unluer, M.J. Tan, Synthesis and characterization of one-part geopolymers for extrusion based 3D concrete printing, J. Clean. Prod. 220 (2019) 610–619. https://doi.org/10.1016/j.jclepro.2019.02.185.

[28] P. Duxson, J.L. Provis, Designing precursors for geopolymer cements, J. Am. Ceram. Soc. 91 (2008) 3864–3869. https://doi.org/10.1111/j.1551-2916.2008.02787.x.

[29] J.L. Provis, Geopolymers and other alkali activated materials: Why, how, and what?, Mater. Struct. Constr. 47 (2014) 11–25. https://doi.org/10.1617/s11527-013-0211-5.

[30] P. Duxson, A. Fernández-Jiménez, J.L. Provis, G.C. Lukey, A. Palomo, J.S.J. Van Deventer, Geopolymer technology: The current state of the art, J. Mater. Sci. 42 (2007) 2917–2933. https://doi.org/10.1007/s10853-006-0637-z.

[31] A.M. Rashad, Metakaolin as cementitious material: History, scours, production and composition-A comprehensive overview, Constr. Build. Mater. 41 (2013) 303–318. https://doi.org/10.1016/j.conbuildmat.2012.12.001.

[32] J.L. Provis, P. Duxson, J.S.J. van Deventer, The role of particle technology in developing sustainable construction materials, Adv. Powder Technol. 21 (2010) 2–7. https://doi.org/10.1016/j.apt.2009.10.006.

[33] F. Pacheco-Torgal, J.P. Castro-Gomes, S. Jalali, Adhesion characterization of tungsten mine waste geopolymeric binder. Influence of OPC concrete substrate surface treatment, Constr. Build. Mater. 22 (2008) 154–161. https://doi.org/10.1016/j.conbuildmat.2006.10.005.

[34] J. Zhou, G. Ye, E. Schlangen, K. van Breugel, Modelling of stresses and strains in bonded

concrete overlays subjected to differential volume changes, Theor. Appl. Fract. Mech. 49 (2008) 199–205. https://doi.org/10.1016/j.tafmec.2007.11.006.
[35] Z. Zhang, X. Yao, H. Wang, Potential application of geopolymers as protection coatings for marine concrete III. Field experiment, Appl. Clay Sci. 67–68 (2012) 57–60. https://doi.org/10.1016/j.clay.2012.05.008.
[36] E. Vasconcelos, S. Fernandes, J.L. Barroso De Aguiar, F. Pacheco-Torgal, Concrete retrofitting using metakaolin geopolymer mortars and CFRP, Constr. Build. Mater. 25 (2011) 3213–3221. https://doi.org/10.1016/j.conbuildmat.2011.03.006.
[37] P. Duan, C. Yan, W. Luo, W. Zhou, Effects of adding nano-TiO2 on compressive strength, drying shrinkage, carbonation and microstructure of fluidized bed fly ash based geopolymer paste, Constr. Build. Mater. 106 (2016) 115–125. https://doi.org/10.1016/j.conbuildmat.2015.12.095.
[38] J. Zhou, G. Ye, K. van Breugel, Cement hydration and microstructure in concrete repairs with cementitious repair materials, Constr. Build. Mater. 112 (2016) 765–772. https://doi.org/10.1016/j.conbuildmat.2016.02.203.
[39] D.R. Morgan, Compatibility of concrete repair materials and systems, Constr. Build. Mater. 10 (1996) 57–67. https://doi.org/10.1016/0950-0618(95)00060-7.
[40] L. Courard, T. Piotrowski, A. Garbacz, Near-to-surface properties affecting bond strength in concrete repair, Cem. Concr. Compos. 46 (2014) 73–80. https://doi.org/10.1016/j.cemconcomp.2013.11.005.
[41] F. Pacheco-Torgal, Z. Abdollahnejad, S. Miraldo, S. Baklouti, Y. Ding, An overview on the potential of geopolymers for concrete infrastructure rehabilitation, Constr. Build. Mater. 36 (2012) 1053–1058. https://doi.org/10.1016/j.conbuildmat.2012.07.003.
[42] E.N.B.S. Júlio, F.A.B. Branco, V.D. Silva, Concrete-to-concrete bond strength. Influence of the roughness of the substrate surface, Constr. Build. Mater. 18 (2004) 675–681. https://doi.org/10.1016/j.conbuildmat.2004.04.023.
[43] W. Dong, W. Li, Z. Tao, K. Wang, Piezoresistive properties of cement-based sensors : Review and perspective, Constr. Build. Mater. 203 (2019) 146–163. https://doi.org/10.1016/j.conbuildmat.2019.01.081.
[44] A. Lasia, Electrochemical Impedance Spectroscopy and its Applications, Springer, 2014. https://doi.org/10.1007/978-1-4614-8933-7.
[45] M. Chiarello, R. Zinno, Electrical conductivity of self-monitoring CFRC, Cem. Concr. Compos. 27 (2005) 463–469. https://doi.org/10.1016/j.cemconcomp.2004.09.001.
[46] B. Han, X. Guan, J. Ou, Electrode design, measuring method and data acquisition system of carbon fiber cement paste piezoresistive sensors, Sensors Actuators, A Phys. 135 (2007) 360–369. https://doi.org/10.1016/j.sna.2006.08.003.
[47] N. Van Meurs, Temperature Dependence of the Conductivity of Electrolyte Solutions, Nature. 182 (1958) 1532–1533. https://doi.org/10.1038/1821532a0.
[48] K.J.D. MacKenzie, M.J. Bolton, Electrical and mechanical properties of aluminosilicate inorganic polymer composites with carbon nanotubes, J. Mater. Sci. 44 (2009) 2851–2857. https://doi.org/10.1007/s10853-009-3377-z.
[49] M. Perry, M. Saafi, G. Fusiek, P. Niewczas, Geopolymeric thermal conductivity sensors for surface-mounting onto concrete structures, (2016).
[50] B. Zareiyan, B. Khoshnevis, Interlayer adhesion and strength of structures in Contour Crafting - Effects of aggregate size, extrusion rate, and layer thickness, Autom. Constr. 81 (2017) 112–121. https://doi.org/10.1016/j.autcon.2017.06.013.
[51] B. Zareiyan, B. Khoshnevis, Effects of interlocking on interlayer adhesion and strength of structures in 3D printing of concrete, Autom. Constr. 83 (2017) 212–221. https://doi.org/10.1016/j.autcon.2017.08.019.
[52] Q. Sun, Y. Peng, H. Cheng, Y. Mou, Z. Yang, D. Liang, Direct ink writing of 3D cavities for direct plated copper ceramic substrates with kaolin suspensions, Ceram. Int. 45 (2019) 12535–12543. https://doi.org/10.1016/j.ceramint.2019.03.191.
[53] G. Franchin, P. Scanferla, L. Zeffiro, H. Elsayed, A. Baliello, G. Giacomello, M. Pasetto, P. Colombo, Direct ink writing of geopolymeric inks, J. Eur. Ceram. Soc. 37 (2017) 2481–2489. https://doi.org/10.1016/j.jeurceramsoc.2017.01.030.

[54] Q. Sun, J. Liu, H. Cheng, Y. Mou, J. Liu, Y. Peng, Fabrication of 3D structures via direct ink writing of kaolin / graphene oxide composite suspensions at ambient temperature, Ceram. Int. 45 (2019) 18972–18979.
[55] T.T. Le, S.A. Austin, S. Lim, R.A. Buswell, A.G.F. Gibb, T. Thorpe, Mix design and fresh properties for high-performance printing concrete, Mater. Struct. Constr. 45 (2012) 1221–1232. https://doi.org/10.1617/s11527-012-9828-z.
[56] T.T. Le, S.A. Austin, S. Lim, R.A. Buswell, R. Law, A.G.F. Gibb, T. Thorpe, Hardened properties of high-performance printing concrete, Cem. Concr. Res. 42 (2012) 558–566. https://doi.org/10.1016/j.cemconres.2011.12.003.
[57] S. Chaves Figueiredo, C. Romero Rodríguez, Z.Y. Ahmed, D.H. Bos, Y. Xu, T.M. Salet, O. Çopuroğlu, E. Schlangen, F.P. Bos, An approach to develop printable strain hardening cementitious composites, Mater. Des. 169 (2019). https://doi.org/10.1016/j.matdes.2019.107651.
[58] H. Alghamdi, S.A.O. Nair, N. Neithalath, Insights into material design, extrusion rheology, and properties of 3D-printable alkali-activated fly ash-based binders, Mater. Des. 167 (2019) 107634. https://doi.org/10.1016/j.matdes.2019.107634.
[59] S. Ketel, G. Falzone, B. Wang, N. Washburn, G. Sant, A printability index for linking slurry rheology to the geometrical attributes of 3D-printed components, Cem. Concr. Compos. 101 (2019) 32–43. https://doi.org/10.1016/j.cemconcomp.2018.03.022.
[60] B. Panda, S.C. Paul, N.A.N. Mohamed, Y.W.D. Tay, M.J. Tan, Measurement of tensile bond strength of 3D printed geopolymer mortar, Meas. J. Int. Meas. Confed. 113 (2018) 108–116. https://doi.org/10.1016/j.measurement.2017.08.051.
[61] M. Xia, J.G. Sanjayan, Methods of enhancing strength of geopolymer produced from powder-based 3D printing process, Mater. Lett. 227 (2018) 281–283. https://doi.org/10.1016/j.matlet.2018.05.100.
[62] F. Bos, R. Wolfs, Z. Ahmed, T. Salet, Additive manufacturing of concrete in construction: potentials and challenges of 3D concrete printing, Virtual Phys. Prototyp. 11 (2016) 209–225. https://doi.org/10.1080/17452759.2016.1209867.
[63] J.G. Sanjayan, B. Nematollahi, M. Xia, T. Marchment, Effect of surface moisture on inter-layer strength of 3D printed concrete, Constr. Build. Mater. 172 (2018) 468–475. https://doi.org/10.1016/j.conbuildmat.2018.03.232.
[64] S.H. Bong, B. Nematollahi, A. Nazari, M. Xia, J. Sanjayan, Method of optimisation for ambient temperature cured sustainable geopolymers for 3D printing construction applications, Materials (Basel). 16 (2019). https://doi.org/10.3390/ma12060902.
[65] M. Xia, J. Sanjayan, Method of formulating geopolymer for 3D printing for construction applications, Mater. Des. 110 (2016) 382–390. https://doi.org/10.1016/j.matdes.2016.07.136.
[66] H. Alghamdi, N. Neithalath, Synthesis and characterization of 3D-printable geopolymeric foams for thermally efficient building envelope materials, Cem. Concr. Compos. 104 (2019).
[67] J. Zhong, G.X. Zhou, P.G. He, Z.H. Yang, D.C. Jia, 3D printing strong and conductive geo-polymer nanocomposite structures modified by graphene oxide, Carbon N. Y. 117 (2017) 421–426. https://doi.org/10.1016/j.carbon.2017.02.102.
[68] B. Panda, M.J. Tan, Experimental study on mix proportion and fresh properties of fly ash based geopolymer for 3D concrete printing, Ceram. Int. (2018) 0–1. https://doi.org/10.1016/j.ceramint.2018.03.031.
[69] B. Panda, M.J. Tan, Experimental study on mix proportion and fresh properties of fly ash based geopolymer for 3D concrete printing, Ceram. Int. 44 (2018) 10258–10265. https://doi.org/10.1016/j.ceramint.2018.03.031.
[70] L.J. van der Pauw, A method of measuring specific resistivity and and Hall effect of discs of arbitrary shape, Philips Res. Reports. 13 (1958) 1–9.
[71] B. Standard, Products and systems for the protection and repair of concrete structures - Test methods - Measurement of bond strength by pull-off, (1999).
[72] C. Dupuy, J. Havette, A. Gharzouni, N. Texier-Mandoki, X. Bourbon, S. Rossignol, Metakaolin-based geopolymer: Formation of new phases influencing the setting time with the use of additives, Constr. Build. Mater. 200 (2019) 272–281. https://doi.org/10.1016/j.conbuildmat.2018.12.114.

[73] N. Roussel, Rheological requirements for printable concretes, Cem. Concr. Res. 112 (2018) 76–85. https://doi.org/10.1016/j.cemconres.2018.04.005.

[74] L. Courard, Adhesion of repair systems to concrete : influence of interfacial topography and transport phenomena, Mag. Concr. Res. 57 (2005) 273–282. https://doi.org/10.1680/macr.57.5.273.64285.

[75] L. Courard, R. Degeimbre, A capillary action test for the investigation of adhesion in repair technology, Can. J. Civ. Eng. 30 (2004) 1101–1110. https://doi.org/10.1139/l03-061.

[76] H. Beushausen, N. Bester, The influence of curing on restrained shrinkage cracking of bonded concrete overlays, Cem. Concr. Res. 87 (2016) 87–96. https://doi.org/10.1016/j.cemconres.2016.05.007.

[77] P. Payakaniti, S. Pinitsoontorn, P. Thongbai, V. Amornkitbamrung, Electrical conductivity and compressive strength of carbon fiber reinforced fly ash geopolymeric composites, Constr. Build. Mater. 135 (2017) 164–176. https://doi.org/10.1016/j.conbuildmat.2016.12.198.

[78] V.A. Nunes, P.H.R. Borges, C. Zanotti, Mechanical compatibility and adhesion between alkali-activated repair mortars and Portland cement concrete substrate, Constr. Build. Mater. 215 (2019) 569–581. https://doi.org/10.1016/j.conbuildmat.2019.04.189.

[79] Z. Zhang, X. Yao, H. Zhu, S. Hua, Y. Chen, Activating process of geopolymer source material: Kaolinite, J. Wuhan Univ. Technol. Sci. Ed. 24 (2009) 132–136. https://doi.org/10.1007/s11595-009-1132-6.

[80] D.G. Soltan, V.C. Li, A self-reinforced cementitious composite for building-scale 3D printing, Cem. Concr. Compos. 90 (2018) 1–13. https://doi.org/10.1016/j.cemconcomp.2018.03.017.

[81] M. Vaysburd, B. Bissonnette, R. Morin, Practice and Quality Assurance, in: B. Bissonnette, L. Courard, D.W. Fowler, J.-L. Granju (Eds.), Bond. Cem. Mater. Overlays Repair, Lining or Strength. Slabs or Pavements, Springer, Dordrecht Heidelberg London New York, 2011: pp. 157–170. https://doi.org/10.1007/978-94-007-1239-3.

[82] B. Han, S. Ding, X. Yu, Intrinsic self-sensing concrete and structures: A review, Meas. J. Int. Meas. Confed. 59 (2015) 110–128. https://doi.org/10.1016/j.measurement.2014.09.048.

[83] S.W. Tang, X.H. Cai, Z. He, W. Zhou, H.Y. Shao, Z.J. Li, T. Wu, E. Chen, The review of pore structure evaluation in cementitious materials by electrical methods, Constr. Build. Mater. 117 (2016) 273–284. https://doi.org/10.1016/j.conbuildmat.2016.05.037.

[84] P. Gu, P. Xie, J.J. Beaudoin, R. Brousseau, A.C. impedance spectroscopy (I): A new equivalent circuit model for hydrated portland cement paste, Cem. Concr. Res. 22 (1992) 833–840. https://doi.org/10.1016/0008-8846(92)90107-7.

[85] V. Feliu, J.A. Gonzalez, C. Andrade, S. Feliu, Equivalent circuit for modelling the steel-concrete interface. I. Experimental evidence and theoretical predictions, Corrision Sci. 40 (1998) 975–993.

[86] J. Sobhani, M. Najimi, Electrochemical impedance behavior and transport properties of silica fume contained concrete, Constr. Build. Mater. 47 (2013) 910–918. https://doi.org/10.1016/j.conbuildmat.2013.05.010.

[87] R. Pouhet, M. Cyr, R. Bucher, Influence of the initial water content in flash calcined metakaolin-based geopolymer, Constr. Build. Mater. 201 (2019) 421–429.

[88] J. Silfwerbrand, H. Beushausen, L. Courard, Bond, in: B. Bissonnette, L. Courard, D.W. Fowler, J.-L. Granju (Eds.), Bond. Cem. Mater. Overlays Repair, Lining or Strength. Slabs or Pavements, RILEM State-of-the-Art Reports 3, 2011: pp. 51–79. https://doi.org/10.1007/978-94-007-1239-3.

[89] S. Lim, R.A. Buswell, P.J. Valentine, D. Piker, S.A. Austin, X. De Kestelier, Modelling curved-layered printing paths for fabricating large-scale construction components, Addit. Manuf. 12 (2016) 216–230. https://doi.org/10.1016/j.addma.2016.06.004.